On the origins of backscattered solar wind energetic neutral hydrogen from the Moon and Mercury

François Leblanc, Robin Deborde, D. Tramontina, E. Bringa, Jean-Yves Chaufray, S. Aizawa, Ronan Modolo, L. Morrissey, A. Woodson, Sébastien Verkercke, et al.

On the origins of backscattered Solar Wind Energetic Neutral Hydrogen from the Moon and Mercury

Leblanc F.[1], Deborde R.[1], Tramontina D.[2], Bringa E.[2], Chaufray J.Y.[3], Aizawa S.[4], Modolo R.[3], Morrissey L.[5], Woodson A.[6] , Verkercke S.[1] and Dukes C.[6]

[1] LATMOS/CNRS, Sorbonne Université, Paris, France.

[2] CONICET and Facultad de Ingeniería - Universidad de Mendoza, Mendoza, 5500, Argentina.

[3] LATMOS/CNRS, Université Versailles Saint Quentin, Guyancourt, France.

[4] IRAP, Toulouse, France.

[5] Memorial University, Canada.

[6] University of Virginia, Charlottesville, USA.

Abstract: The surfaces of planetary airless bodies are directly bombarded by solar particles. The most abundant of those particles are solar wind protons. In the case of the Moon, many in situ observations have shown that a significant portion of these incident solar-wind protons are backscattered as energetic neutral hydrogen atoms (ENA). Measurements of the energy flux distribution of these neutral particles provide a clue regarding the processes occurring in the surface regolith when impacting protons collide with the surface grains.

In this work, we developed a model to describe the fate of protons through a regolith model and compared our results with Chandrayaan-1 ENA measurements. We combined a Monte Carlo approach to reconstruct the motion of these particles into a layer of grains with molecular dynamics to parametrize the interaction of an incident proton with a grain. Using simultaneous measurements of the incident plasma by Chandrayaan-1 SWIM, this detailed modelling allowed us to analyse the measurements performed by the Chandrayaan-1 CENA instrument when the Moon is in the solar wind and in the Earth's magnetosheath, and to highlight what could control the flux and energy properties of these backscattered neutral hydrogen particles. Predictions of the intensity and shape of the backscattered neutral hydrogen distribution at Mercury are derived from this calculation.

I Introduction

The surfaces of planetary airless bodies, such as the Moon, are directly bombarded by solar wind protons, giving rise to surface bound exospheres (Stern 1999). IBEX-HI (McComas et al. 2009) observed that a significant portion of these incident protons (between 10 to 20%) are backscattered from the Moon as Energetic Neutral Atoms (ENA) . The global value was later confirmed to be 9% using the IBEX-Lo (Rodriguez et al. 2012; Funsten et al. 2013; Allegrini et al. 2013) instrument on board the IBEX mission. Using the Chandrayaan-1 Energetic Neutral Atom Instrument (CENA) sensor of the Sub-keV Atom Reflecting Analyzer (SARA, Barabash et al. 2009) on board the Chandrayaan-1 Lunar orbiter (Goswami and Annadurai,2009), Wieser et al. (2009) estimated that up to 20% of the solar wind protons incident on the Lunar equator might be backscattered as ENAs, a value which was later confirmed as being equal to 19% by Futaana et al. (2012). Vorburger et al. (2014) also reported that backscattered He neutral atoms amount to only 0.14% of the total number of incident He^{++} solar wind ions. Based on IBEX measurements, Funsten et al. (2013) reported an ENA albedo varying from 20% for slow solar wind to 8% for fast solar wind, a value confirmed by Allegrini et al. (2013) who found a value of 10% on an average.

These backscattered ENAs essentially follow a Solar Zenith Angle (SZA) dependency (Wieser et al. 2009; Saul et al. 2013) directly proportional to the incident solar wind proton flux with the exception of the regions of local crustal magnetic fields. In these particular regions, Chandrayaan-1/CENA instruments observed a complex spatial structure of the reflected backscattered protons suggesting that the incident solar wind flow is deflected by the local magnetic field anomaly (Futaana et al. 2013). Backscattered ions were also observed by SELENE/MAP-PACE (Saito et al. 2008) corresponding to a percentage of the incident solar wind protons between 0.1 and 1%, a value later confirmed by ARTEMIS (Lue et al. 2018) which reported the percentage of backscattered protons between 0.5% for a solar wind speed of 300 km/s and 0.3% for a solar wind speed of 500 km/s.

In Futaana et al. (2012) and Wieser et al. (2009), a measurement of the differential energy flux of the backscattered hydrogen ENAs was provided by Chandrayaan-1/CENA covering an energy range from

25 eV up to 10 keV on three consecutive orbits in July 2009 and February 2009. Futaana et al. (2012) used observations performed when the Moon was in the solar wind whereas Wieser et al. (2009) used data observed in the magnetosheath of the Earth. Despite a difference in flux of one order of magnitude, both distributions peak around 200 eV, an energy much larger than for hydrogen atoms that would be sputtered from the surface (Eckstein and Behrisch 2007), with an extended plateau from 200 eV to the lowest energy covered by CENA and a quick decrease of the flux from 200 eV up to a few keV (to be compared to the typical 1 keV energy of the incident solar wind protons). Such distribution was interpreted by Futaana et al. (2012) as the evidence of "*multiple collisions off surfaces of regolith grains*". Wieser et al. (2009) measured an ENA backscattered flux larger than Futaana et al. (2012) in agreement with the conclusions by Allegrini et al. (2013) showing that ENA backscattered fluxes measured in the magnetosheath are larger on average than the same flux measured when the Moon is in the Solar wind. Allegrini et al. showed that back scattering hydrogen fluxes were more intense in the magnetosheath for energies below ~0.6 times the Solar Wind energy by analyzing many spectra of the IBEX sensors normalized by the average conditions. These authors concluded that higher low-energy release occurs when the plasma Mach number is lower. Rodriguez et al. (2012), using IBEX/IBEX-Lo, reported a similar energy distribution of the hydrogen ENAs with an extended plateau down to the limit of detection of IBEX-Lo at 14 eV when the Moon was in the Solar Wind or in the magnetosheath. We are not aware of any measurement by IBEX or Chandrayan-1 of ENA when the Moon is inside the Earth magnetosphere. More recently, Zhang et al. (2020) using the Advanced Small Analyzer for Neutrals on board the Chinese CHang'E-4 rover reported a hydrogen ENA albedo of 32% above 30 eV.

Hodges (2011) published the first complete modelling of the interaction of solar wind protons with a regolith using a Monte Carlo approach that followed atoms in the Lunar surface, including representative solar wind fluxes. That study stated a neutralization probability of the impacting protons equal to 91% to fit with the observed 1% of particles reflected as ions (Saito et al. 2008) and a

45% average energy loss during each collision between an incident atom and a grain. Hodges (2011) completed a detailed analysis of the measurements reported by Wieser et al. (2009) and found an excellent agreement between simulation and observations taking into account some corrections (Wieser et al. 2011) to the originally published (Wieser et al. 2009) differential energy flux and Chandrayaan-1/CENA instrumental energy response.

In this paper, we employ a similar approach as Hodges (2011) by modelling incident solar wind particles penetrating a regolith model to reproduce Chandrayaan-1/CENA measurements. However, in this study we use a combined Monte Carlo/Molecular Dynamics approach. First, Monte Carlo modelling is used to reconstruct the motion of these particles into a layer of grains representative of the lunar surface regolith. Next, we then use molecular dynamics (MD) to properly describe the interaction of an incident proton with a grain—in particular the energy loss and angular redistribution during particle-grain collisions. This detailed modelling approach allows us to accurately analyse the measurements performed by the Chandrayaan-1 CENA instrument and to highlight what could control the flux and the energy of these backscattered hydrogen atoms. We also extrapolate the results of this modelling in order to predict what should be the observed flux of hydrogen ENA at Mercury (Lue et al. 2017; Orsini et al. 2021). Section II describes the two models used to perform our modelling whereas section III presents the results of this modelling and section IV concludes this paper.

II Model

The model developed to describe the fate of the solar wind protons in the upper layer of the Lunar surface can be decomposed into two parts:

- a calculation of the trajectory of an individual particle in a layer composed of grains (defined as single-crystal unit within a polycrystalline material, section II.1),
- a calculation of the interaction of a particle with a grain (section II.2)

II.1 The fate of protons through a regolith

The regolith is described by an ensemble of 70000 spherical grains with a diameter of 1.52 µm in 70 μm^3, yielding a density of ~35%, which is close to the expected grain density at the Moon's surface (Sarantos et al. 2021). Typical distance between grains is of the order of 3 µm. This size of grain is small with respect to the typical size of grain at the Moon surface (Sarantos et al. 2021), but might be representative of the top layer of the surface. Such an effect will be addressed in a forthcoming paper. To be able to compare directly our results to data deduced from Chandrayaan-1/CENA measurements, we used Chandrayaan-1/SWIM energy distribution of the incident solar wind protons measured simultaneously for three orbits on the 6^{th} of February 2009 (Wieser et al. 2011) but corrected by a factor 0.55 as suggested by Hodges (2011) based on a comparison between SWIM and ACE measurements. For Futaana et al. (2012), typical solar wind conditions during the 17 and 18 July 2009 corresponded to a mean solar wind speed of 290 – 320 km/s and a solar wind density of 4.8 – 6.0 cm^{-3}. The solar wind conditions are used to generate individual proton test-particles, each of them representative of a large number of real particles as defined by a weight. The initial velocity of these test particles is determined from a mean solar wind bulk velocity component pointing towards the surface (radial direction) to which an isotropic thermal velocity component is added. The trajectory of the particle is calculated below the surface up to the moment the particle either reemerges from the surface—in which case we registered its velocity, weight and charge—or reaches an energy smaller than 10 eV. At each time step we determine if the particle encounters a grain (see Figure 1), in which case a parameterization based on the molecular dynamics modelling described in section II.2 is used to determine the energy and velocity direction of the reemitted particle. We neglect the effects of the gravity fields of the Moon and the Earth as well as any electro-magnetic forces that could act on the trajectory of the particle. Indeed, since the typical distance between two collisions is of only few µms (equivalent to the inter-granular distance), the true trajectory between two collisions would closely approximate a straight line. Moreover, for the energy range considered in this work (between 10 eV and few keV), the change in energy is largely dominated by particle-grain collisions, while that due to gravity and electro-magnetic fields is negligible. The time step was optimized to reduce the calculation

duration but was also kept small enough to properly describe all collisions between particle and grain (typically of the order of 0.3 picosecond). The timestep was also adjusted to determine accurately the position of each grain-particle collision at the surface of the grains.

To describe the trajectory of a test particle just after its collision with a grain, we need to define several parameters:

- the position of the impact at the surface of the grain and the velocity of the test particle in the frame of the grain;

- the charge state of the particle, for which we used Hodges (2011) assumption that neutralization is very efficient and corresponds to a probability of 91% that an incident ion will be neutralized after encountering the regolith;

- the probability that a particle is implanted or absorbed into the grains (section II.2), which is taken into account by reducing the weight of the test-particle by the percentage absorbed in the grain;

- the energy of the particle after collision, determined using a Molecular Dynamics model (see section II.2),

- the direction of the velocity vector after collision, which is determined by the Molecular Dynamics model as described in section II.2.

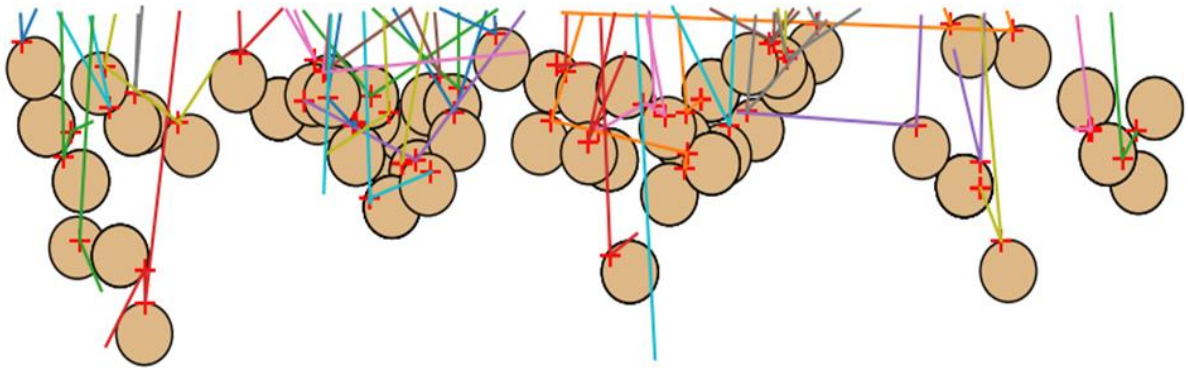

Figure 1: *Cut along a vertical slice of the modelled regolith displaying the trajectories of several test-particles through a regolith composed of grains of 1.52 µm diameter (brown circles) with a density of 35%. The red crosses represent the position of the impact of each test-particle on a grain surface.*

Thus, when a particle collides with a grain, the new velocity vector of the particle is calculated at the position of the impact of the particle with the grain, neglecting the nanometer distance travelled by the particle into the grain.

II.2 Grain – proton interactions

To account for proton-grain interaction, we used an atomistic Molecular Dynamics model that describes the proton interaction with a grain composed of a set of atoms as illustrated in Figure 2.

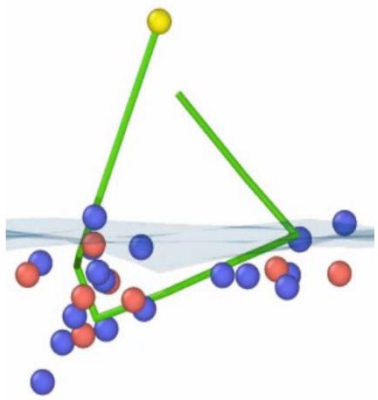

Figure 2: *Trajectory (green lines) of a proton (yellow atom) interacting with a SiO_2 regolith grain. The blue circles represent O atoms whereas the red circles represent Si atoms. The typical spatial scale of this trajectory is few nm. This trajectory is significantly different from the often assumed single specular collision. Only atoms acquiring an energy larger than 0.2 eV are shown.*

Classical molecular dynamics simulations solve Newton's equations for a set of interacting particles. We use the open-sourced software LAMMPS (Thompson et al. 2022) to model the impact of protons on a silica surface. Interactions between atoms are described by Reactive Force Field (ReaxFF; Smith et al. 2017), which includes several different contributions like screened Coulomb interactions, and allows for charge exchange and various bonding environments. ReaxFF has been extensively used for silica simulations (Fogarty et al. 2010, Yu et al. 2016; Joseph et al. 2021). We use a standard procedure to build a silica sample, starting from a quartz crystal, molten, then cooled, and finally relaxed to obtain a glassy sample. Details of this procedure are given in the Supplementary Material (SM). The final density of this amorphous sample is 2.21 g/cm^3, in agreement with experiments (Quenneville et al. 2010) and simulation results (Fogarty et al. 2010). The partial correlation functions $g_{ij}(r)$ shown in SM

Figure S1, compare extremely well with the ones obtained previously by similar simulations (Nayir et al. 2019; Onodera et al. 2020). In order to simulate bombardment, a free surface is created by generating a vacuum region above the sample, and then relaxing that new structure. This leads to some reconstruction at the surface, as expected. The final sample is approximately a cube, 7 nm side, and has 24000 atoms (8000 Si, 16000 O). Lateral periodic boundary conditions were used. Atoms in the bottom 0.2 nm were fixed, and the velocity of protons reaching this layer was set to zero, in order to mimic a much deeper regolith sample. There is approximately 1.5 nm of vacuum above and below the sample, to model bombardment.

Incident protons are approximated as neutral hydrogen atoms. We found that reflection typically involves many collisions in the upper few nm of the silica sample, and fast neutralization is expected, as discussed above, at this low impact energy. Due to the high computational cost of charge exchange, it was included in the sample preparation, but we turned this off during the thousands of impact simulations carried out. This set-up neglects backscattering of H^+, which is expected to be more than one order of magnitude lower than H backscattering. Random impact points are selected for each bombardment, leading to different local environments around the impact and various outcomes, including the possibility of reflection and sputtering of target atoms. MD simulations were carried out adding a close range Ziegler, Biersack and Liitmark potential (ZBL; Ziegler et al. 2004) to ReaxFF, for atoms closer than 0.1 nm. Details about the implementation of ZBL appear in Appendix 1. Simulations used an adaptive time step, and finished after about 2 ps, when the proton reached the bottom of the sample and was considered absorbed, or when it was reflected and reached the top of the simulation box. 500 events were simulated for each (energy, angle) combination. This was enough to ensure reflection coefficients with an error of less than 10%. We simulated independent impacts, always with the same pristine sample, but changing the impact site for a given impact energy and angle. Future studies might include cumulative impacts where incident ions change the nature of the target. Figure 2 shows the outcome of a typical single simulation.

In order to fully characterize the proton-grain collisions, we need to specify three parameters, as follows:

- For each of the simulated energies/angles, we computed the number of protons reflected from the grain (see as an example Figure 2). Five sets of simulations were performed at 25 eV, 50 eV, 200 eV, 500 eV, 800 eV and 1200 eV, for an incident angle of 45° (Figure 3a). The dependency of this reflection with respect to the energy was then deduced and fitted with a function described below. Simulations for several angles in the range 20-80 degrees were performed at 25 eV and 500 eV, in order to derive angular dependency, see Figure 3b. Combining the two dependencies, we found a best fit of the reflection probability with respect to both incident angle θ and energy E following:

$$P_{reflection}(\theta, E) = (0.603 \times e^{-1.372\times10^{-3}\times E})^{(cos\theta)^{0.8}} \quad (1)$$

Figure 3 includes simulations using SRIM2013. We obtained results using 10^5 protons, impacting a regolith of density of 2.21 g cm^{-3} with a lattice binding energy of 1 eV for Si and 8 eV for O, and a surface binding energy for Si and O atoms of 0.5 eV. These binding energies were chosen to reproduce mean values in the MD simulations, where there is a wide distribution of lattice and surface binding energies, as recently discussed for Na in a silicate (Killen et al. 2022). SRIM2013 results are 30%-50% lower than MD results at low energy, but there is a cross-over near 1.2 keV. SRIM cross-sections were derived from experimental results starting at a few keV, and are not expected to be reliable below a few keV [Posselt1995]. Binary Collision Approximation (BCA) codes like SRIM suffer from difficulties describing surface structure and binding, although there are improvements with respect to SRIM2013 (Szabo et al. 2022).

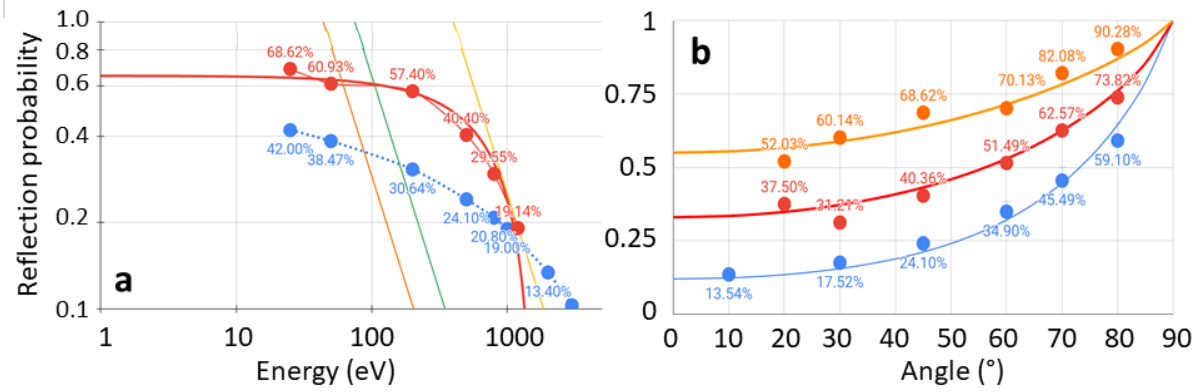

Figure 3: Panel a: *Reflection probability of a proton colliding with a grain as a function of its incident energy at an angle of 45° with respect to the surface normal. MD simulations (red circles), SRIM (blue circles, joined by a dotted line), and proposed fit using Eq. 1 (thick solid red line). WS model fits, assuming different targets (thin solid lines): SiO_2 (orange), Si (green), O (yellow). Panel b: Reflection probability as a function of the incident angle using SRIM (500 eV protons, blue) and MD simulations (500 eV, red circles, and 25 eV, orange circles). Lines correspond to fits with a BW model (Bøttiger et al. 1973). R_0=0.12, b=0.9 (blue line). R_0=0.33, b=0.8 (red line), and R_0=0.25, b=0.83. (orange line).*

Figure 3a also includes the WS model (Weissmann and Sigmund 1973) for which the reflection probability R follows $R=1.05\times\varepsilon^{-3/2}$ *with* $\varepsilon = \left(\frac{M_2 E}{M_1+M_2}\right) / \left(\frac{Z_1 Z_2 e^2}{a}\right)$ *with* M_1, M_2, Z_1, Z_2, a, *and* e being the mass of the proton, the mass of the molecules in the regolith, the atomic number of the proton, the atomic number of the molecules in the regolith, the Bohr radius and the elementary charge respectively. The WS model assumes a single bouncing collision for reflection and is intended as a rough guide only. Reflection probability goes to 1 as energy goes down, and this requires the inclusion of multiple collisions. Thomas et al. (1992) proposed an alternative equation for R in terms of scaled energy, but it requires six different fit parameters. Figure 3b also includes SRIM results for 500 eV. For 25 eV incident energy SRIM would be unreliable at energies so close to the binding energy, where many-body, not binary, collisions would be crucial, and no results are included. Note that the decrease of reflection as angle decreases is stronger for BCA than for MD simulations. We also show lines

corresponding to a Bøttiger-Winterbon (BW) model of the form $R=R(\theta=0)^{\cos(\theta)^{\wedge}b}$, with b=0.8 for MD simulations and b=0.9 for SRIM. Discrepancies between BCA codes and experimental sputtering yields for H against SiO_2 were noted in a recent study (Schaible et al. 2017).

- If the particle is re-ejected from the grain, we estimated its energy after collision using the simulated energy distribution of the backscattered protons derived from four simulations performed at an angle of 45° for 25 eV, 200 eV, 500 eV and 800 eV (Figure 4). We linearly interpolated between these four profiles to derive the energy of the re-ejected particles for any incident energy.

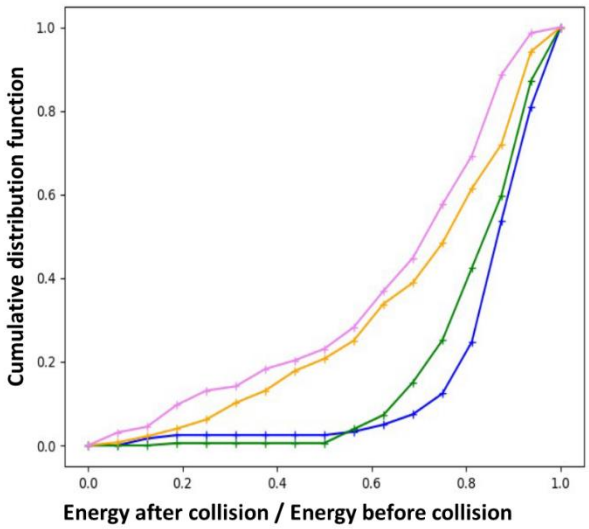

Figure 4: *Cumulative energy distribution of a hydrogen atom reflected from a single regolith grain. Blue, green, orange and pink lines are for 800 eV, 500 eV, 200 eV and 25 eV incident proton energy at 45°.*

- The last parameter needed to fully describe the velocity vector of the backscattered particle is its angle with respect to the normal to the surface. Here again, according to the results obtained with the Molecular Dynamics simulations, below 60° incident angle of the incident primary or secondary particles with respect to the normal to the surface, we used a Gaussian function centered around the incident angle and with a Full Width Half Maximum (FWHM) of

18° whereas above 60° a Rayleigh distribution centered on the incident angle and with a FWHM following a relation like $\sigma(\theta) = -0.0163\theta + 1.48$ is used.

III Results

III.1 Hydrogen Energetic Neutral Atoms backscattered from the Moon surface

Approximately 700000 test particles were tracked for each simulation, incorporating Futaana et al. solar wind conditions and Wieser et al. Magnetosheath conditions for which 20.4% and 18.9% of the test particles were reflected while 79.6% and 80.8% were absorbed respectively. In both cases, less than 1% of protons reached energies lower than 10 eV before being absorbed. Each test particle underwent 4 collisions with the grain, on average, before exiting the simulation and the maximum penetration depth was of only 20 µm with more than 95% of the incident protons being deposited at a regolith depth less than 6 µm.

In Fig. 5 we show the differential energy flux of hydrogen ENA as measured by the Chandrayaan-1/CENA instrument and reported by Futaana et al. (2012) (black points in panel a) and Wieser et al. (2011) (black points in panel b). CENA measurements below 30 eV are shown even if reported by Futaana et al. (2012) as highly uncertain. Our simulated fluxes of hydrogen ENA are shown in red and our simulated proton backscattered fluxes in orange. We simply summed in each energy band of CENA the weight of the particle divided by the energy width and by 2π steradian (assuming an isotropic ejection). We also reproduced the solar wind proton flux used for both simulations in blue. The simulated proton backscattered fluxes might be influenced by the charge state of the surface (Halekas et al. 2010), in particular at low energy, the dayside surface potential being able to reach few tens of V.

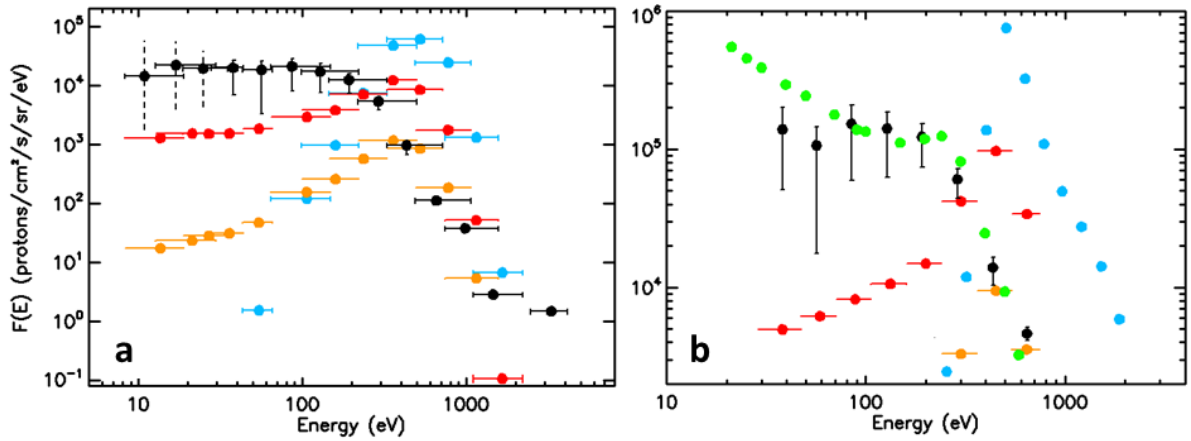

Figure 5: Panel a: *black points: measured differential energy flux of ENA by Chandrayaan-1/CENA (Futaana et al. 2012). Red points: simulated differential energy flux of backscattered H from the Moon surface. Blue points: measured solar wind incident proton differential energy flux (Chandrayaan-1/SWIM, Futaana et al. 2012). Orange points: simulated differential energy flux of backscattered protons. Panel b: black points: measured differential flux of ENA by Chandrayaan-1/CENA (Wieser et al. 2011). Red point: simulated differential energy flux of backscattered H from the Moon surface. Blue point: measured solar wind incident proton differential energy flux (Chandrayaan-1/SWIM, Wieser et al. 2011). Orange point: simulated differential energy flux of backscattered protons. Green points: simulated differential energy flux by Hodges (2011).*

As shown in Figure 5, we found a better agreement between simulation (red symbols) and observation (black symbols) in the case of the observation performed when the Moon was in the Solar Wind (panel a) than when the Moon was in the magnetosheath (panel b). As a matter of fact, both measured fluxes are surprisingly similar in shape despite different incident protons fluxes. Hodges et al. (2011) modelled the panel b case using a corrected Solar Wind flux, decreased by a factor 0.55 over that of Wieser et al. (2011)—a correction we also adopted for the panel b simulation. The flux measured by SWIN on board Chandrayaan-1 and displayed in blue points on Figure 5b and used to simulate the backscattered flux is therefore probably not accurate enough and might explain part of the discrepancy between observation and simulation. In Figure 5 panel b, we also plot the simulated differential energy flux of

the backscattered hydrogen atoms as modeled by Hodges (2011). The very good agreement between the observation and Hodges model was obtained by adopting a mean energy loss of 45% at each collision, an energy loss not predicted by our Molecular Dynamics simulation as displayed in Figure 4. The backscattered flux simulated by our model (red points) peaks at the right order of magnitude around 200 eV and decreases at a rate close to that observed for energies > 200 eV. However, our simulation displays a decrease of the backscattered population at lower energies that is not seen in the observation nor in Hodges (2011) simulation. As a matter of fact, Futaana et al. (2012) pointed out that the 60% rate for backscattered hydrogen ENA above 25 eV suggested by Hodges (2011) was not consistent with their estimated range of 9–24%, which is in good agreement with our present estimate. This suggests that a scenario with an increased intensity of the differential flux below 100 eV is less likely. Moreover, IBEX reported several observations with better sensitivity at low energy than CENA suggesting the existence of such a plateau in the Solar Wind (Allegrini et al. 2013), a suggestion reinforced by the most recent measurements by ASAN/Chang'E 4 (Zhang et al. 2020). The origin of this plateau in flux below 200 eV appears to be partly associated with the Solar Wind flux distribution. Comparing the simulated back-scattered hydrogen energy distribution displayed in Figure 5a to the simulated one in Figure 5b, there is a clear difference in the shape of the backscattered distribution at low energy. The main difference between these two simulations being the input Solar Wind distribution, it is clearly one of the parameters controlling the shape of the backscattered distribution at low energy. This plateau should also be populated by back-scattered hydrogen atoms coming from incident Solar Wind protons that lost a significant part of their energy through the regolith. Since our simulation clearly underestimates this plateau, it implies that we do not succeed in properly describing this population of particles losing more than 80% of their initial energy before being reemitted. One possible explanation is our choice to describe the surface upper layer with smaller grains than are actually present on the Moon's surface. Both grain size and aggregation porosity will affect backscattering (Szabo et al. 2022). This concern will be explored further in a forthcoming paper.

Allegrini et al. (2013) also highlighted that the energy peak of the backscattered neutral hydrogen flux usually occurred at an energy equal to 60% of the Solar Wind incident energy. In the case of the measurements done when the Moon was in the Solar wind (Figure 5a), the Solar Wind flux peaked at an energy around 500 eV and our simulated backscattered flux peaked at an energy of 320 eV, in good agreement with the conclusion of Allegrini et al. (2013). In the case of the magnetosheath measurements (Figure 5b), our simulation suggested a peak in energy of the backscattered hydrogen atoms slightly smaller than the incident energy (at 450 eV for an incident flux peaking at 500 eV). This suggests that, in our simulation, the energy at which the backscattered neutral flux peaks is not only related to the incident Solar wind energy but also to its temperature. The measured, backscattered-proton flux and the backscattered-proton flux modeled by Hodges (2011) both peaked at an energy equal to ~220 eV, significantly smaller than what we should have expected given the conclusion of Allegrini et al. (2013). This difference again suggests that the input used for our simulation displayed in Figure 5b is probably not accurate enough.

Since energetic hydrogen atoms can also be produced through sputtering of the regolith by incident protons, we considered the possibility of a sputtered contribution to the observed CENA differential flux. Based on the study of Eckstein et al. (2007), we estimated the efficiency of hydrogen sputtering from the grains by incident protons to be the same as that for incident Li atoms. The angular distribution of the ejecta was chosen to follow a $\cos(\theta)$ relation while the energy distribution falls off as E^{-2} above 10 eV, which is the range of energy considered here. According to Eckstein et al. (2007), the yield varies from 0.2 at a normal incidence to a maximum of 2 around 75° incidence angle and is only marginally dependent on the incidence energy within the typical solar wind energy range. These values are rather large since classical values for the yield of protons impacting a regolith are closer to 0.1 (see as an example Schaible et al. 2017). Even for the very unrealistic case in which the hydrogen abundance in the grain is one, the sputtered population would not exceed 10^3 hydrogen atoms/(cm^2 s

sr eV) at 10 eV and would quickly decrease for larger energy. Therefore, it is very unlikely that the observed flux has a significant contribution from sputtering as concluded also by Futaana et al. (2012).

As stated above 83.5% of the incident protons are absorbed in the grain. Our model can provide a first estimate of the depth at which these incident protons will get implanted. According to Figure 6, most of the protons are implanted in the first layer of grains between 0 and 5 µm below the surface. This result is consistent with the relatively limited number of collisions, on average, of the incident protons in the regolith.

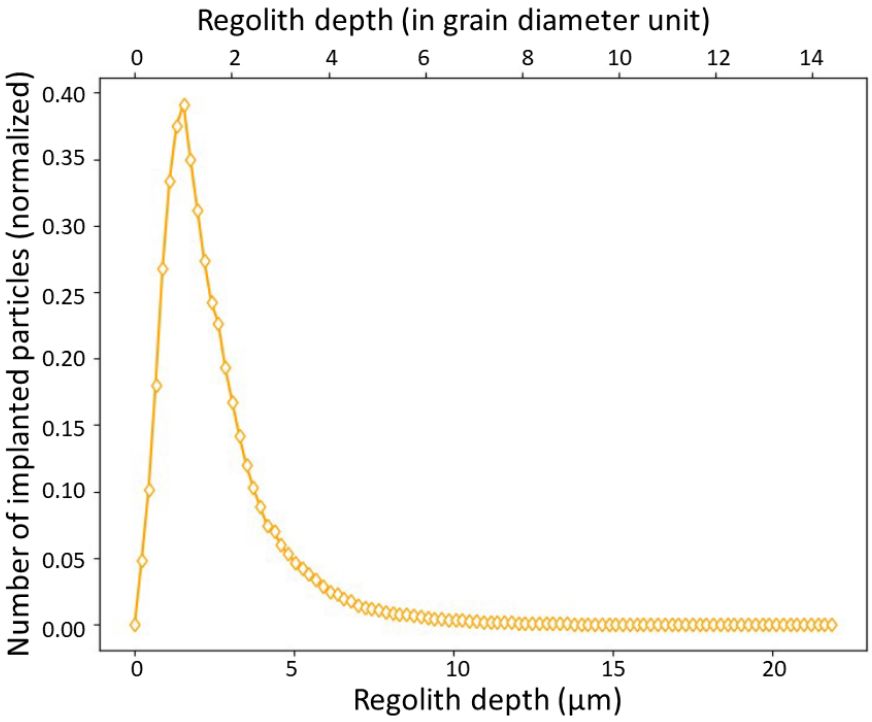

Figure 6: *Depth implantation of the incoming solar wind proton in the regolith. Horizontal lower scale in µm, horizontal top scale in grain diameter unit.*

III.2 Hydrogen Energetic Neutral Atoms backscattered from Mercury surface

Following the results of our modelling of the backscattered hydrogen ENA from the Moon surface, we simulated what could be the flux of backscattered hydrogen ENA from Mercury's surface. Aizawa et al. (2022) simulated the solar wind proton flux penetrating the magnetosphere of Mercury and impacting

the planetary surface for various solar wind conditions. In Figure 7, panel a, we displayed the flux of protons impacting the surface in the case of nominal solar conditions as simulated by Aizawa et al. (2022). From this flux and the energy and angular distributions of the reflected ENAs simulated on the Moon, we reconstructed the ejection rate and the energy and angular distributions of hydrogen ENA from the surface of Mercury. We used the same approach described in sections II.1 and II.2 with the assumption that both regoliths have similar albedo. In panel b of Figure 7, the ratio of ejected hydrogen ENA to incident protons is displayed with values between 5% and 25%. When comparing panels a and b, we don't find a direct relation between impacting and backscattered flux because, as shown in Figure 3, the rate of backscattered particles depends on the energy and angle of the incident particles.

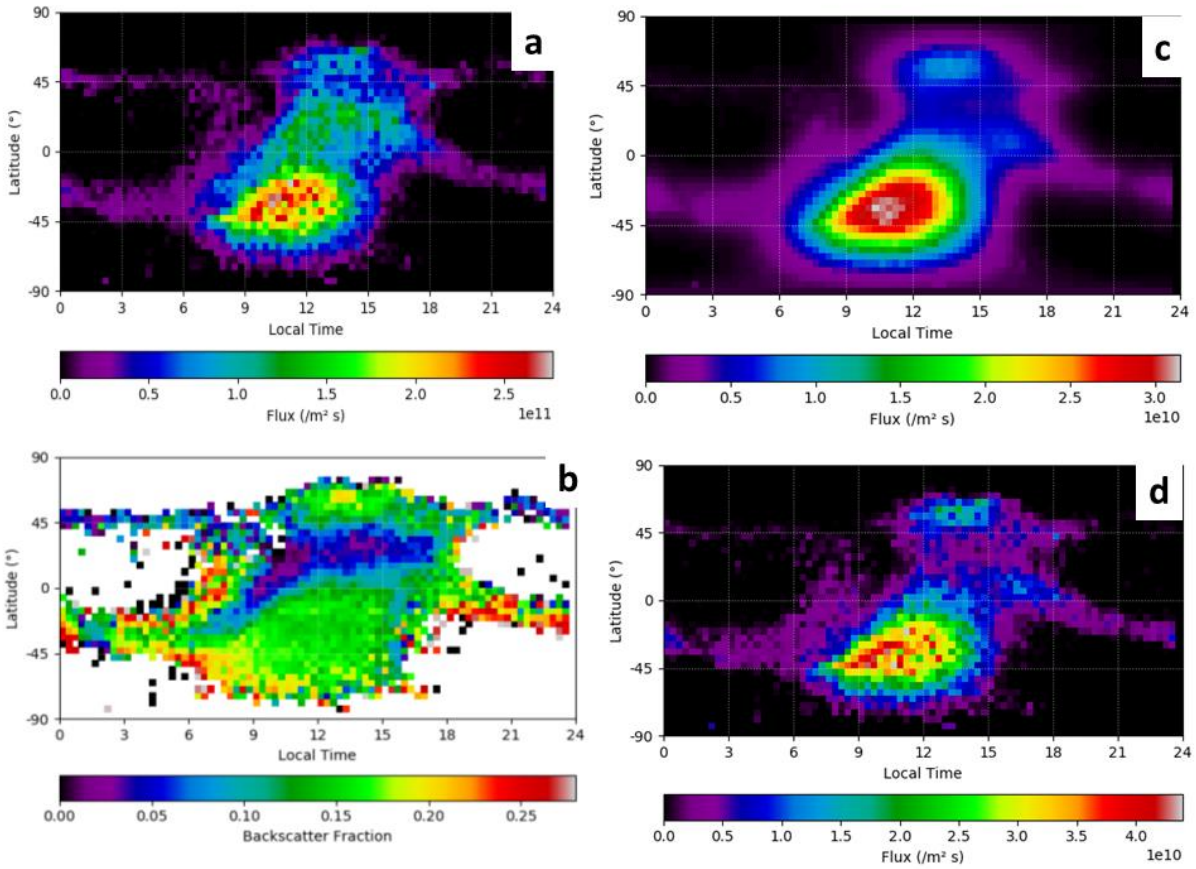

Figure 7 : *Panel a : Precipitating flux of H^+ Solar Wind particles impacting the surface for nominal solar wind conditions, a Solar Wind speed of 450 km/s, a Solar Wind density of 50 cm^{-3} and an Interplanetary Magnetic Field of 17 nT with nominal Parker Spiral orientation at Mercury (Aizawa et al. 2022). Panel b: Backscattered fraction of the incident protons as hydrogen ENA (taking into account incident energy*

and angle of the incident protons). Panel c: reconstructed hydrogen ENA flux at 400 km in altitude. Panel d: backscattered flux of proton at the surface.

In Figure 7c, we reconstructed the potential rate of backscattered hydrogen ENA that could be measured at 400 km in altitude above Mercury's surface, the typical periapsis altitude of MPO/BepiColombo (see appendix 2 regarding the mathematical approach used for this calculation). As shown on this panel, the shape of the simulated hydrogen ENA does not accurately reflect panels a and b. It is a spatially blurred image of the precipitation flux at the surface of Mercury (panel d), essentially because the ENAs flux comes from a large portion of the surface, but probably less blurred than an image of the precipitation that could be reconstructed from magnetic field measurements at 400 km above the surface, highlighting the interest of ELENA/SERENA on board BepiColombo (Orsini et al. 2021).

IV Conclusion

Solar wind protons have been observed to be back-scattered from the Moon's surface by the Chandrayaan-1 ENA instrument (Wieser et al. 2009; Futaana et al. 2012) as well as by the IBEX Lo instrument (McComas et al. 2009), showing an unexpected high rate of protons backscattered as neutral hydrogen atoms. The Chandrayaan-1 ENA instrument was also able to measure the energy distribution of these particles simultaneously with measurements of the solar wind characteristics.

Using this information, we developed a model describing the fate of protons moving through a Lunar regolith approximated as individual spherical grains. Our model combined a Monte Carlo approach that tracks the motion of atoms in the upper 10–20 µm of the regolith with a Molecular Dynamics approach describing the interaction between individual atoms and grains. Our model reproduced Chandrayaan-1/ENA observations with good agreement in the case of those measurements obtained in the Solar Wind (Futaana et al. 2012), while agreement was less pronounced and in a lesser way in the case of those measurements obtained in the magnetosheath (Wieser et al. 2009).

Lastly, by applying our model to a map of Solar Wind proton precipitation at Mercury we have provided an estimate of backscattered atomic hydrogen flux at the planet's surface and at 400 km altitude, which will coincide with the BepiColombo/Mercury Planetary Orbiter nominal periapsis altitude, thus allowing direct comparison between our estimates and in orbits measurements once the spacecraft arrive at Mercury in 2025 (Orsini et al. 2021).

Acknowledgments: F.L. and J.-Y.C. acknowledge the support by ANR, France of the TEMPETE project (grant ANR-17-CE31-0016) and the support of CNES, France for the BepiColombo mission. This research was supported by the International Space Science Institute (ISSI) in Bern, through ISSI International Team project # 559 ”Improving the Description of Exosphere Surface Interface”. Authors also acknowledge the support of the IPSL data center CICLAD for providing us access to their computing resources and data. Data may be obtained upon request from F. Leblanc (email:francois.leblanc@latmos.ipsl.fr). EMB and DT thank support from PICTO-UUMM-2019-00048 and SIIP-UNCUYO 06/M008-T1.

References

Aizawa S., N. André, M. Persson, R. Modolo, J. Raines, F. Leblanc, J.-Y. Chaufray, Q. Nenon, Escape and precipitation of planetary ions at Mercury under different solar wind conditions, Planet. Space Sci., Submitted, 2022.

Allegrini F., M.A. Dayeh, M.I. Desai, H.O. Funsten, S.A. Fuselier, P.H. Janzen, D.J. McComas, E. Möbius, D.B. Reisenfeld, D.F. Rodríguez M., N. Schwadron, P.Wurz, Lunar energetic neutral atom (ENA) spectra measured by the interstellar boundary explorer (IBEX), Planetary and Space Science, 85, 232-242, 2013.

Allen, M.P. and Tildesley, D.J., 2017. *Computer simulation of liquids*. Oxford university press.

Barabash, S., Bhardwaj, A., Wieser, M., Sridharan, R., Kurian, T., Varier, S., Vijaykumar, E., Abhirami, V., Raghavendra, K.V., Mohankumar, S.V., Dhanya, D.B., Thampi, S., Asamura, K., Andersson, H., Futaana, Y., Holmstr€om, M., Lundin, R., Svensson, J., Karlsson, S., Piazza, R.D., Wurz, P., 2009. Investigation of the solar wind-Moon interaction on board Chandrayaan-1 mission with the SARA experiment. Curr. Sci. 96 (4), 526–532.

Barry P.R., P. Phillip *et al.*, Mechanisms of silicon sputtering and cluster formation explained by atomic level simulations, J. Mass. Spectrum. **49** (2014) 185. https://doi.org/10.1002/jms.3317

Benkhoff, J., Murakami, G., Baumjohann, W. *et al.* BepiColombo - Mission Overview and Science Goals. *Space Sci Rev* 217, 90 (2021). https://doi.org/10.1007/s11214-021-00861- 4

Behrisch, R., Eckstein, W., *Sputtering by Particle Bombardment*. (2007). Springer Berlin Heidelberg. https://doi.org/10.1007/978-3-540-44502-9

Bøttiger J., K.B. Winterbon, Reflection of light ions from solid surfaces, Rad. Eff., 20, 65, (1973). https://doi.org/10.1080/00337577308232267

Cassidy T. and Johnson, R.E. (2005). Monte Carlo model of sputtering and other ejection processes within a regolith. *Icarus*, *176*(2), 499–507. https://doi.org/10.1016/j.icarus.2005.02.013

Dubinskii, A. Y., & Popel, S. I. (2019). Water Formation in the Lunar Regolith. *Cosmic Research*, *57*(2), 79–84. https://doi.org/10.1134/s0010952519020047

Fogarty J.C., H.C. Aktulga *et al.*, A reactive molecular dynamics simulation of the silica-water interface, J. Chem. Phys. 132 2010 174704. https://doi/oeg/0.1063/1.3407433

Funsten, H.O., Allegrini, F., Bochsler, P.A., Fuselier, S.A., Gruntman, M., Henderson, K., Janzen, P.H., Johnson, R.E., Larsen, B.A., Lawrence, D.J., McComas, D.J., Möbius, E., Reisenfeld, D.B., Rodriguez, D., Schwadron, N.A., Wurz, P., 2013. Reflection of solar wind hydrogen from the lunar surface, Journal of Geophysical Research:Planets, 118, 292, http://dx.doi.org/10.1002/jgre.20055.

Futaana, Y., Barabash, S., Wieser, M., Holmström, M., Lue, C., Wurz, P., Schaufelberger, A., Bhardwaj, A., Dhanya, M. B., & Asamura, K. (2012). Empirical energy spectra of neutralized solar wind protons from the lunar regolith. *Journal of Geophysical Research: Planets*, *117*(E5), n/a. https://doi.org/10.1029/2011je004019

Futaana, Y., Barabash, S., Wieser, M., Lue, C., Wurz, P., Vorburger, A., Bhardwaj, A., Asamura, K., 2013. Remote energetic neutral atom imaging of electric potential over a lunar magnetic anomaly. Geophys. Res. Lett. 40, 262–266. https://doi.org/10.1002/grl.50135.

Guénolé J., W.G. Noring *et al.*, Assessment and optimization of the fast inertial relaxation engine (fire) for energy minimization in atomistic simulations and its implementation in Lammps, Comp. Mat. Sci. **175** (2020) 109584. https://doi.org/10.1016/j.commatsci.2020.109584

Goswami, J.N., Annadurai, M., 2009. Chandrayaan-1: India's first planetary science mission to the moon. Current Science 96, 4 25 February

Halekas J.S., Y. Saito, G.T. Delory and W.M. Farrell, New views of the lunar plasma environment, Planet. Space Sci., 2010. https://doi:10.1016/ j.pss.2010.08.011

Hestenes M.R., Stiefel E., Methods of conjugate gradients for solving linear systems, J. Res. Nat. Bur. Std. **49** 6 (1952) 409. http://nvl.nist.gov/pub/nistpubs/jres/049/6/V49.N06.A08.pdf

Hodges, R. R. (2011). Resolution of the lunar hydrogen enigma. *Geophysical Research Letters*, *38*(6), n/a. https://doi.org/10.1029/2011gl046688

Huang, Z., Nomura, K.-i., Morrissey, L. S., & Wang, J. (2022). Molecular dynamics simulation of solar wind implantation in the permanently shadowed regions on the lunar surface. Geophysical Research Letters, 49, e2022GL099333. https://doi. org/10.1029/2022GL099333

Joseph E., N. Swaminathan, Investigation of mechanical properties and dispersion in silica/Styrene Butadiene Rubber (SBR) nanocomposites: A ReaxFF molecular dynamics study, Comp. Mater. Sci. 200 (2021) 110751. doi: 10.1016/j.commatsci.2021.110751

Konnert J.H. *et al.*, Comparison of radial distribution function for silica glass with those for various bonding topologies: Use of correlation function, J. Non-Xtal Solids **53** (1982) 135.

Killen R.M., L.S. Morrissey, M.H. Burger, R.J. Vervack, O.J. Tucker, D.W. Savin, The Influence of Surface Binding Energy on Sputtering in Models of the Sodium Exosphere of Mercury, The Planetary Science Journal **3** (2022) 139. https://iopscience.iop.org/article/10.3847/PSJ/ac67de/pdf

Lue C., Futaana Y. Barabash S., Wieser M., Bhardwaj A., Wurz P. and K. Asamura, Solar Wind scattering from the surface of Mercury: lessons from the Moon, Icarus, 296, 39-48, 2017. http://dx.doi.org/10.1016/j.icarus.2017.05.019

Lue, C., Halekas, J. S., Poppe, A. R., & McFadden, J. P. (2018). ARTEMIS observations of solar wind proton scattering off the lunar surface. Journal of Geophysical Research: Space Physics, 123, 5289–5299. https://doi.org/ 10.1029/2018JA025486

McComas, D. J., et al. (2009), Lunar backscatter and neutralization of the solar wind: First observations of neutral atoms from the Moon, Geophys. Res. Lett., 36, L12104, doi:10.1029/2009GL038794.

Nayir N., A.C.T. van Duin, S. Erkoc, Development of a ReaxFF Reactive Force Field for Interstitial Oxygen in Germanium and Its Application to GeO2/Ge Interfaces, J. Phys. Chem. A 123 (2019) 43031, doi: 10.1021/acs.jpcc.8b08862

Onodera et al. Structure and properties of densified silica glass: characterizing the order within disorder, NPG Asia Materials 12 (2020) .85 https://doi.org/10.1038/s41427-020-00262-z

Orsini, S. and 120 colleagues, SERENA: Particle Instrument Suite for Determining the Sun-Mercury Interaction from BepiColombo, Space Science Reviews 217, 2021. ⟨10.1007/s11214-020-00787-3⟩ - insu-03108958

Posselt M. and K.-H. Heinig, Comparison of BC and MD simulations of low-energy ion implantation, Nucl. Instruments Methods Phys. Res. Sect. B Beam Interact. with Mater. Atoms **102**.(1995) 1 . https://doi.org/10.1016/0168-583X(95)80148-F

Rodríguez, D. F. M., L. Saul, P. Wurz, S. A. Fuselier, H. O. Funsten, D. J. McComas, and E. Möbius (2012), IBEX-Lo observations of energetic neutral hydrogen atoms originating from the lunar surface, Planet. Space Sci., 60(1), 297–303, doi:10.1016/j.pss.2011.09.009.

Saito, Y., Yokota, S., Tanaka, T., Asamura, K., Nishino, M. N., Fujimoto, M., Tsunakawa, H., Shibuya, H., Matsushima, M., Shimizu, H., Takahashi, F., Mukai, T., & Terasawa, T. (2008). Solar wind proton reflection at the lunar surface : Low energy ion measurement by MAP-PACE onboard SELENE (KAGUYA). *Geophysical Research Letters*, *35*(24). https://doi.org/10.1029/2008gl036077

Saul, L., Wurz, P., Vorburger, A., Rodríguez, M.D.F., Fuselier, S.A., McComas, D.J., Möbius, E., Barabash, S., Funsten, H.O., Janzen, P., 2013. Solar wind reflection from the lunar surface: the view from far and near, Planetary and Space Science, 84, 1-4, 2013. http://dx.doi.org/10.1016/j.pss.2013.02.004

Sarantos, M., & Tsavachidis, S. (2021). Lags in Desorption of Lunar Volatiles. *The Astrophysical Journal Letters*, *919*(2), L14. https://doi.org/10.3847/2041-8213/ac205b

Schaible, M. J., Dukes, C. A.,Hutcherson,A.C.,Lee,P.,Collier,M.R.,& Johnson, R. E. (2017). Solar wind sputtering rates of small bodies and ion mass spectrometry detection of secondary ions. Journal of GeophysicalResearch: Planets,122, 1968–1983.https://doi.org/10.1002/2017JE005359

Schaufelberger, A., Wurz, P., Barabash, S., Wieser, M., Futaana, Y., Holmstr¨om, M., Bhardwaj, A., Dhanya, M.B., Sridharan, R., Asamura, K., 2011. Scattering function for energetic neutral hydrogen atoms off the lunar surface. Geophysical Research Letters 38 (22), 1–6, http://dx.doi.org/10.1029/2011GL049362.

Schaufelberger, A., Wurz, P., Barabash, S., Wieser, M., Futaana, Y., Holmström, M., Bhardwaj, A., Dhanya, M. B., Sridharan, R., & Asamura, K. (2011). Scattering function for energetic neutral hydrogen atoms off the lunar surface. *Geophysical Research Letters*, *38*(22), n/a. https://doi.org/10.1029/2011gl049362

R. Smith, K. Jolley, *et al.*, A ReaXFF carbon potential for radiation damage studies, Nucl. Instrum. Met. Phys. Res. B 393 (2017) 49. https://doi.org/10.1016/j.nimb.2016.11.007.

Starukhina, L. (2001). Water detection on atmosphereless celestial bodies : Alternative explanations of the observations. *Journal of Geophysical Research : Planets*, *106*(E7), 14701–14710. https://doi.org/10.1029/2000je001307

Stern, S.A., The lunar atmosphere: history, status, current problems and context, Reviews of Geophysics, 37, 4, 453–491, 1999.

Szabo P. et al. Graphical user interface for SDTrimSP to simulate sputtering, ion implantation and the dynamic effects of ion irradiation. NIMB 522, 47-53 (2022). https://doi.org/10.1016/j.nimb.2022.04.008

Szabo P. et al. (a) Deducing Lunar Regolith Porosity From Energetic Neutral Atom Emission, Geophys. Res. Lett. (2022) 49. https://doi.org/10.1029/2022GL101232.

Thomas, E. W., Janev, R. K., & Smith, J. (1992). Scaling of particle reflection coefficients. Nuclear Instruments and Methods in Physics Research Section B: Beam Interactions with Materials and Atoms, 69(4), 427–436. https://doi.org/10.1016/0168-583x(92)95298-6

Thompson A. P., H. M Aktulga et al., LAMMPS - a flexible simulation tool for particle-based materials modeling at the atomic, meso, and continuum scales, Comp. Phys. Comm 271 (2022) 108171. https://doi.org/10.1016/j.cpc.2021.108171

Quenneville J., R. S. Taylor, A.C.T. van Duin, Reactive Molecular Dynamics Studies of DMMP Adsorption and Reactivity on Amorphous Silica Surfaces, J. Phys. Chem. C 114 (2010) 18894. https://doi.org/10.1021/jp104547u

Vorburger, A., Wurz, P., Barabash, S., Wieser, M., Futaana, Y., Holmstr€om, M., Bhardwaj, A., Asamura, K., 2014. First direct observation of sputtered lunar oxygen. J. Geophys. Res. 119 (2), 709–722. https://doi.org/10.1002/2013JA019207.

Weissmann R. and P. Sigmund, Sputtering and backscattering of keV light ions bombarding random targets, Rad. Eff. 19 (1973) 7. https://doi.org/10.1080/00337577308232208

Wieser, M., Barabash, S., Futaana, Y., Holmström, M., Bhardwaj, A., Sridharan, R., Dhanya, M. B., Wurz, P., Schaufelberger, A., & Asamura, K. (2009). Extremely high reflection of solar wind protons as neutral hydrogen atoms from regolith in space. *Planetary and Space Science*, *57*(14-15), 2132–2134. https://doi.org/10.1016/j.pss.2009.09.012

Wieser, M., Barabash, S., Futaana, Y., Holmström, M., Bhardwaj, A., Sridharan, R., Dhanya, M. B., Wurz, P., Schaufelberger, A., & Asamura, K. (2011), Erratum to ‘‘Extremely high reflection of solar wind protons as neutral hydrogen atoms from regolith in space’’ [Planet. Space Sci. 57 (2009) 2132–2134], Planet. Space Sci., 59, 798-799, 2011. doi:10.1016/j.pss.2011.01.016

Wurz, P., Rohner, U., Whitby, J. A., Kolb, C., Lammer, H., Dobnikar, P., & Martín-Fernández, J. A. (2007). The lunar exosphere : The sputtering contribution. *Icarus*, *191*(2), 486–496. https://doi.org/10.1016/j.icarus.2007.04.034

Yu Y., B. Wang, *et al.*, Revisiting silica with ReaxFF: Towards improved predictions of glass structure and properties via reactive molecular dynamics, J Non Cryst. Sol. 443 (2016) 148 https://doi.org/10.1016/j.jnoncrysol.2016.03.026

Zhang, A., Wieser, M., Wang, C., Barabash, S., Wang, W., Wang, X., et al. (2020). Emission of energetic neutral atoms measured on the lunar_surface by Chang'E-4. Planetary and Space Science, 189(15). https://doi.org/10.1016/j.pss.2020.104970

Ziegler J.F., SRIM-2003, Nucl. Instr. Meth. B 219-220 (2004) 1027. https://doi.org/10.1016/j.nimb.2004.01.208

Appendix 1 Atomistic simulation details

MD simulation preparation. The amorphous sample is built with the usual method of melting a quartz crystal and then cooling the melt relatively fastly. We started from a perfect cubic monocrystalline sample with quartz structure with 7 nm size, containing 24000 atoms (8000 Si, 16000 O). Periodic boundaries are set initially in all directions. The sample creation process consists of several steps:

(I) under an NVT ensemble (constant number of particles N, volume V and temperature T): (a) heat the sample to 7000 K; (b) hold the melt during 25 ps; (c) Cool down to 300 K during 25 ps. (II) minimize the box energy with conjugate gradient, and then minimize energy with the constrain that pressure should be zero. (III) under a NPT ensemble (isothermic-isobaric), with P=0 bar, (a) heat the sample again to 7000 K; (b) hold the melt during 25 ps; (c) Cool down to 300 K during 25 ps; (d) hold at 40 K during 25 ps.

We use charge equilibration every 10000 steps. This procedure is shorter than other similar procedures used in the literature, but ensures correct density (2.2 g/cm^3) and correct pair correlation functions g(r), as shown in Fig. S1. There are several silica simulations showing similar g(r) (Fogarty et al. 2010, Barry et al. 2014, Nayir et al. 2019; Onodera et al. 2020).

There are two issues which are not typically discussed regarding silica samples: some relaxation procedures to obtain experimental densities might lead to large atomic stress or to a large population of atoms with positive binding energy. These two issues might lead to artificial results under irradiation. Our final atomic stress is less than 0.1 Pa and only a few O atoms display positive binding energy. The role of surface binding energies was recently discussed for Na-containing silicate sputtering (Killen et al. 2022).

Two free surfaces are created by simply removing the periodic boundaries along z, and allowing 1.5 nm of vacuum above and below the silica. The upper surface will be bombarded and the bottom surface will be kept fixed during bombardment, as detailed below. The structure with surfaces was minimized using a conjugate gradient and FIRE minimization (Guénolé et al. 2020), followed by another

10 ps run under the NVE microcanonical ensemble (constant number of particles N, volume V and energy E) before bombardment, which has to be simulated under NVE conditions.

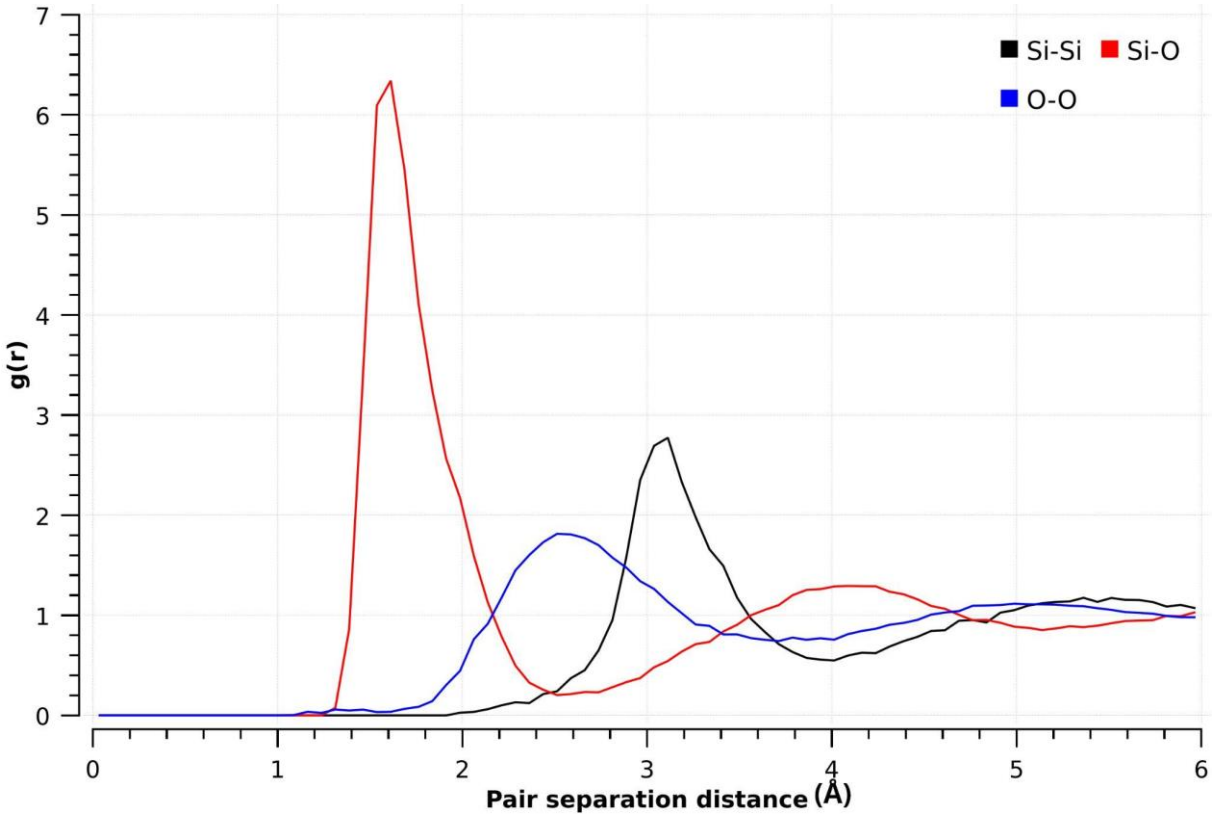

Figure S1: *Pair correlation function $g_{ij}(r)$ for amorphous SiO_2 model, showing that correlation disappears beyond 3rd nearest neighbors. This result agrees with similar studies.*

The potential used for irradiation is ReaxFF (Fogarty et al. 2010), with the addition of a ZBL potential for energetic interactions. ZBL requires $\mathbf{R_{inner}}$, the distance where the switching function begins, and $\mathbf{R_{outer}}$, where ZBL goes to zero. We employed 0.085 nm and 0.1 nm as $\mathbf{R_{inner}}$ and $\mathbf{R_{outer}}$.

Some projectiles did penetrate all the way to the bottom of the sample. Since our goal was to study ion reflection, not the ion range, atoms in the bottom 0.2 nm of the sample were frozen, setting their velocities and the forces acting on them to zero. Reflected or sputtered atoms reaching the top of the box were also frozen, after their velocity vectors were saved to calculate energy and angular distributions.

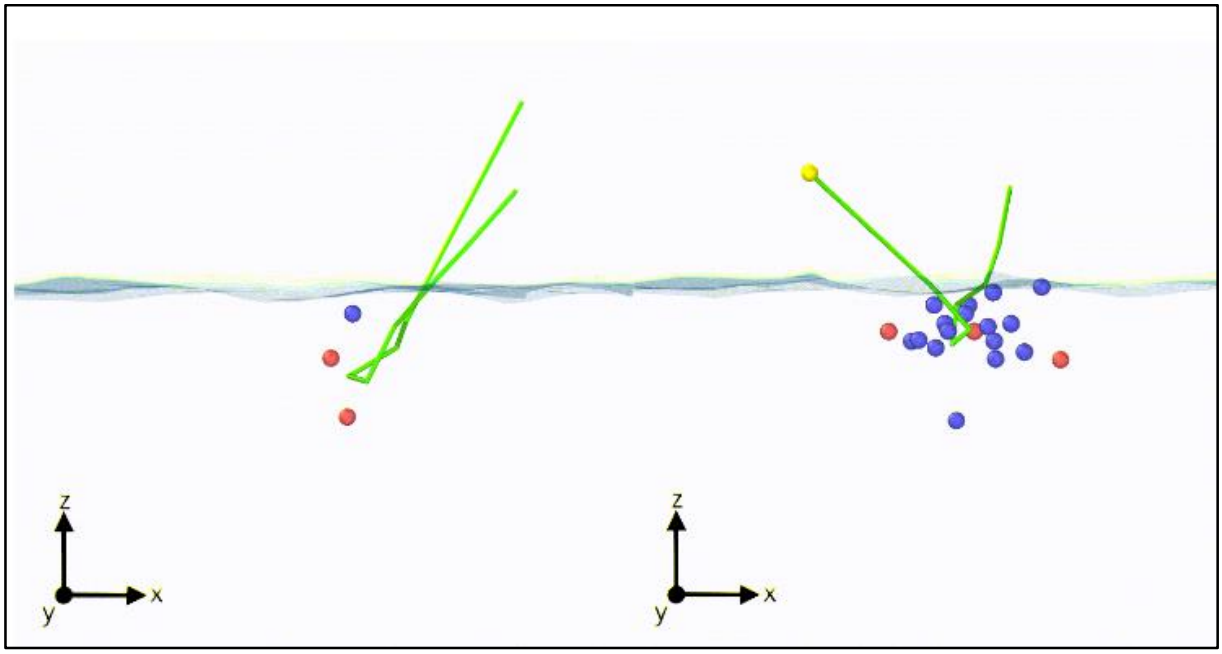

Figure S2: *Trajectories of two H^+ impacting the regolith at 25 eV 45°. A filter for particles with kinetic energy smaller than 0.2 keV was applied. Size of particles are not representative. Colors: yellow: H, blue: Si, red: O. Ion parameters are the same and only differ in the impact position coordinates. This leads to differences on the energy transferred and final state of the ion, including reflection for the cases shown.*

Appendix 2

To compute the ENAs flux received by a detector at a position M in the exosphere, we consider an instrument pointing towards the surface (nadir direction) with a field of view larger than the cone intercepting the planet (Figure S3) and a surface area $a << H_M^2$ and a $<< R^2$, where R is the radius of Mercury and H_M the altitude of M. The MSO altitude, latitude and longitude of M are noted (H_M, λ_M, ς_M) and the MSO cartesian coordinates are noted (x_M, y_M, z_M).

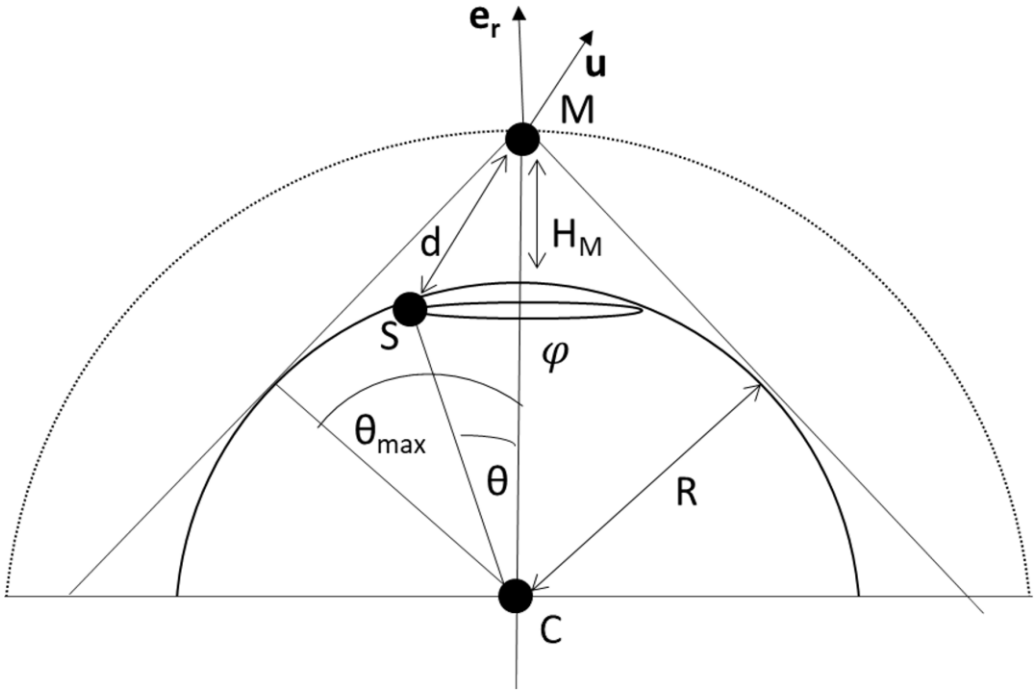

Figure S3 : Geometry of the ENA observation

We assume an isotropic emission of H-ENAs from the surface i.e :

$$\Phi(S) = 2\pi I_0(S, \boldsymbol{u}) \qquad \text{A1}$$

where $I_0(S,\mathbf{u})$ is the number of reflected H-ENAs per second, per area unit and per steradian at position S on the surface and in the direction **u** and Φ(S) is the number of reflected H-ENAs per second, per area unit (the integral of I_0 over all the direction **u** in the semi-hemisphere above the surface).

The number of ENAs received on the surface of the detector at M coming from the elementary surface dS at S is

$$dN = I(\theta,\varphi, \mathbf{u})\omega dS \qquad \text{A2}$$

$\omega = (\mathbf{u}.a\mathbf{e_r})/d^2$ is the solid angle of the surface of the detector (area *a*) seen from S, **u** is the unit vector parallel to **SM**, $\mathbf{e_r}$ the unit vector opposite to the nadir direction (i.e. : the radial unit vector) *d* the distance SM and $dS = R^2 \sin\theta d\theta d\varphi$ the surface element of Mercury. The position

of S at the surface of Mercury is parametrized by the two angles (θ, φ), where θ is the angle between **CM** and **CS**, and φ the azimuthal angle around the direction **CM** (Figure S3).

Only the portion of the surface delimited by the cone $\theta < \theta_{max}=\text{acos}[R/R+H_M)]$, shown in Figure S3, can be seen by the detector. The total number of ENAs received by the detector is therefore the integral of dN on the « visible » surface of Mercury:

$$N = R^2 a \int_{\varphi=0}^{\varphi=2\pi} \int_{\theta=0}^{\theta=\text{acos}(\frac{R}{R+H_M})} I(\theta,\varphi,\vec{\mathbf{u}}) \frac{(\vec{u}\cdot\vec{e_r})}{d^2} sin\theta d\theta d\varphi \qquad \text{A3}$$

The flux F(M) = N/a received by the detector at M is given by

$$F(M) = \frac{R^2}{2\pi} \int_{\varphi=0}^{\varphi=2\pi} \int_{\theta=0}^{\theta=a\cos(\frac{R}{R+H})} \Phi(\theta,\varphi) \frac{(\vec{u}\cdot\vec{e_r})}{d^2} sin\theta d\theta d\varphi \qquad \text{A4}$$

Simple geometric calculations can be used to express *d* and ($\mathbf{u}.\mathbf{e_r}$) as function of θ, R and H_M to finally obtain :

$$F(M) = \frac{b^2}{2\pi} \int_{\varphi=0}^{\varphi=2\pi} \int_{\theta=0}^{\theta=\text{acos}(\frac{b}{b+1})} \Phi(\theta,\varphi) \left[\frac{b(1-cos\theta)+1}{[1+2b(b+1)(1-cos\theta)]^{3/2}}\right] sin\theta d\theta d\varphi \qquad \text{A5}$$

where $b = R/H_M$ is a dimensionless parameter.

Two asymptotic cases can be considered :

Case 1 : The observer is very far from Mercury ($b << 1$). Then $\theta_{max} \sim \pi/2$, and F is given by

$$F(M) = \frac{b^2}{2\pi} \int_{\varphi=0}^{\varphi=2\pi} \int_{\theta=0}^{\theta=\pi/2} \Phi(\theta,\varphi) sin\theta d\theta d\varphi \qquad \text{A6}$$

In this case, the flux F(M) decreased as $\sim 1/H_M^2$ (at a given λ_M and ς_M) as expected from the ENAs flux conservation.

Case 2 : the observer is very close to the surface of Mercury ($b >> 1$). In this case $\theta_{max} << 1$ and we can consider a uniform flux coming from the surface just below the detector: $\Phi(\theta=0)$. The integral can be calculated analytically (e.g. https://www.wolframalpha.com) to obtain :

$$F(M) = \frac{b^2\Phi(\theta=0)}{2\pi}\frac{2\pi}{(1+b)^2}\left[G(\text{acos}\left(\frac{b}{1+b}\right)) - G(0)\right] \quad \text{A7}$$

with

$$G(\theta) = -\frac{cos\theta + b(cos\theta - 1)}{\sqrt{1+2b(1+b)(1-cos\theta)}} \quad \text{A8}$$

Because G(0) = -1, G(acos[b/(1+b)]) = 0 , and b >> 1, we find :

$$F(M) = \Phi(\theta = 0) \quad \text{A9}$$

Numerical expression

Given, the position M in the exosphere of Mercury, we can link θ and φ to the MSO spatial coordinates of M by considering the new basis defined by

$$\overrightarrow{z'} = \frac{\overrightarrow{CM}}{\|\overrightarrow{CM}\|} = \frac{1}{\sqrt{x_M^2+y_M^2+z_M^2}}\begin{pmatrix} x_M \\ y_M \\ z_M \end{pmatrix} \quad \text{A10}$$

and **x'** and **y'** defined to have a direct orthogonal basis. In this new frame θ and φ are the usual spherical coordinates and the position of S given by

$$\overrightarrow{CS} = Rcos\theta\overrightarrow{z'} + Rsin\theta cos\varphi\overrightarrow{x'} + Rsin\theta sin\varphi\overrightarrow{y'} \quad \text{A11}$$

can be calculated in MSO frame from the spatial coordinates (x_M, y_M, z_M) of M and any parameters θ, φ.

The surface of Mercury is discretized, denoting K and L the number of elements for θ and φ. Noting K_{lim} the largest integer k fullfilling the condition $\cos(\theta_k) > b/(1+b)$. The numerical approximation of F is given by :

$$F(M) = \frac{b^2}{2\pi}\sum_{l=1}^{l=L}\sum_{k=1}^{k=K_{lim}}\int_{\varphi=\varphi_l}^{\varphi=\varphi_{l+1}}\int_{\theta=\theta_k}^{\theta=\theta_{k+1}}\Phi(\theta,\varphi)\left[\frac{b(1-cos\theta)+1}{[1+2b(b+1)(1-cos\theta)]^{3/2}}\right]sin\theta d\theta d\varphi \quad \text{A12}$$

Assuming a constant flux $\Phi(\theta_k,\varphi_l)$ for each surface elements $[\theta_k, \theta_{k+1}]x[\varphi_l, \varphi_{l+1}]$. The integrals can be computed analytically (see above) to obtain the numerical expression :

$$F(M) = \frac{b^2}{2\pi(1+b)^2}\sum_{l=1}^{l=L}\sum_{k=1}^{k=K_{lim}} \Phi(\theta_k,\varphi_l)(\varphi_{l+1}-\varphi_l)[G(\theta_{k+1})-G(\theta_k)] \quad \text{A13}$$

What is known is not $\Phi(\theta_k,\varphi_l)$ but $\Phi(\lambda_S,\varsigma_S)$ instead. The spherical coordinates of S in MSO : $(R, \lambda_S, \varsigma_S)$ can be derived from θ_k, φ_l from Eq. A11 and the **x'**,**y'**, and **z'** vectors (e.g. Eq. A10 for **z'**). Note that the assumption of constant flux on $[\theta_k, \theta_{k+1}]x[\varphi_l, \varphi_{l+1}]$ requires to have a resolution in θ_k, φ_l better or equal to the resolution in λ_S and ς_S for Φ. This equation was used to compute the received flux (Fig. 6c) for a detector at any MSO latitude and longitude at H_M = 400 km (b~ 6.1) with a resolution of 4.5° in all angular variables.